Scatterometer Ground Processing Review for Gyro-Less Operations

Xavier Neyt, Pauline Pettiaux and Marc Acheroy

Royal Military Academy, Brussels, Belgium

ABSTRACT

The scatterometer on-board of the ERS spacecraft is range-gated, in opposition to Seasat/Nscat scatterometers that are Doppler filtered. It can thus admit some Doppler frequency shift in the returned echo. However, the bandwidth of the filter on-board of the ERS satellite limits the Doppler shift that can be tolerated on the returned echo data. For these reasons, the ERS spacecraft needs to be yaw-steered in order to minimize the residual Doppler shift. Due to a malfunction of several of the on-board gyroscopes used to govern the attitude of the ERS-2 spacecraft, precise yaw steering of the spacecraft cannot be guaranteed anymore. This paper reviews modifications to the existing processing chain that are needed to be able to process the data acquired by the ERS-2 spacecraft in degraded attitude mode, so called zero-gyro mode (ZGM). The main modification is the introduction of the on the fly estimation of the yaw angle as input to a model of the acquisition geometry. This paper also details how the yaw angle is estimated from the received raw data by measuring the residual Doppler frequency shift. Finally, several improvements such as the impact of an increased spatial resolution of the backscattering coefficients are also discussed.

Keywords: Scatterometry, optimal filters, attitude estimation

1. INTRODUCTION

The scatterometer on board ERS-2 works at 5.3GHz and is range gated. Due to the limited bandwidth of the on-board anti-aliasing filter, the satellite needs to be yaw-steered in order to minimize the Doppler frequency shift on the received echo signal.

Due to gyroscopes malfunction, a new attitude and orbit control system is used on-board ERS-2 since the beginning of 2001. The new piloting mode of the spacecraft, termed zero-gyro mode (ZGM), does not use any of the gyroscopes. The remaining attitude sensors (a Digital Earth Sensor and a Digital Sun Sensor) are used to pilot the spacecraft. While the pitch and roll attitude angles have almost nominal values, the yaw angle can exhibit large variations around its nominal yaw-steering mode (YSM) value.

The on-board and on-ground compensation of the Doppler frequency shift is computed to correct the shift introduced by a spacecraft in perfect YSM. When the spacecraft is not in YSM, a significant part of the spectrum of the received echo is shifted outside the pass-band of the on-ground low-pass filter, resulting in an underestimation of the backscattered energy. Moreover, yaw angle variations have obviously geometric implications.

For these two reasons, the algorithm currently used to process the scatterometer data is not able to handle data acquired in non-nominal YSM. This is the main motivation for a review of the scatterometer ground processing. As part of the reviewing process, other enhancements such as the increase of the spatial resolution of the output product were considered.

The first section will summarize the main functional blocks of the existing processing chain. The upgraded processing chain will be detailed in the next section, together with some of the enhancements introduced.

Further author information: (Send correspondence to Xavier Neyt) E-mail: Xavier.Neyt@rma.ac.be, Telephone: +32 2 737 6473, Address: Signal and Image Center, Electrical Engineering Dept, Royal Military Academy, 30 av de la Renaissance, B-1000 Brussels, Belgium

2. EXISTING GROUND PROCESSOR

2.1. Block diagram

The ground processing of the scatterometer data aims at computing the backscattering coefficients (σ^0) from raw echo data and originally consists in the following steps: a time filtering and a detection followed by spatial averaging.

The aim of the time filtering essentially consists in increasing the signal-to-noise ratio by reducing the pass-band of the system using a low-pass filter. The on-board Doppler shift compensation only roughly compensates the frequency shift experienced by the signal. A finer compensation is performed on-ground in order to center the spectrum of the received signal inside the pass-band of the subsequent low-pass filter. Since the on-board anti-aliasing filter is a Bessel filter, the signal inside the pass-band is slightly attenuated. This has to be compensated before shifting the spectrum of the signal. This compensation is performed in the block called "amplitude correction". Next the signal is demodulated (envelope detection) and the non-linearity of the on-board ADC is corrected for. The internal calibration correction and the normalization respectively aim at correcting the received signal for a varying emitted energy and removing the effect of the range and incidence angle on the received echo power.

The spatial averaging aims at further reducing the variability of the measurements by averaging the measured samples over a certain window, resulting in the final spatial resolution of the measurements.

Figure 1 presents a simplified version of the block diagram of the existing processor, where only the major blocks were kept. The full block diagram can be found in.[1]

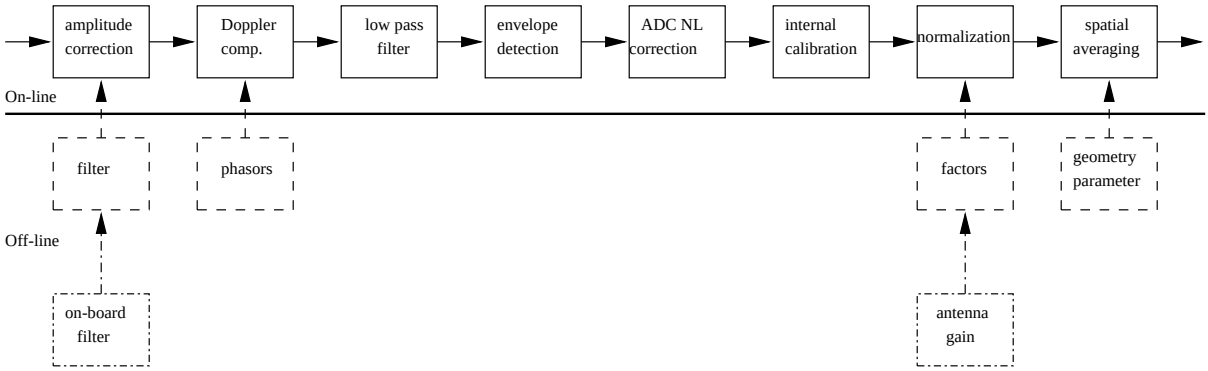

Figure 1. Simplified block diagram of the old processor. This includes both on-line processing, performed while processing the actual measured data and off-line processing, performed once, the resulting look-up tables being uploaded in the operational processor.

Most of the elements of this processing relied heavily on the use of look-up tables that were pre-computed for a perfectly yaw-steered spacecraft. For instance, the factor used to normalize the backscattered energy was pre-computed for a particular orbit and a particular attitude (yaw angle). This was made possible by the fact that the spacecraft always had the same attitude along all orbits. Since all the orbits having the same repeat cycle are the same, one table per repeat cycle was sufficient. Due to the fact that the spacecraft's actual yaw angle is not a priori known and not periodic anymore, look-up tables can not be used anymore. For these reasons, a simple adaptation of the existing satellite simulator software, used to compute these look-up tables, was not sufficient. Moreover, since the yaw angle had to be estimated from the data, a full redesign of the ground processor was deemed necessary.

3. NEW GROUND PROCESSOR

3.1. Block diagram

The most striking difference between the block diagram of the existing processor (fig. 1) and that of the new processor (fig. 2) are first the fact that the modules that pre-computed off-line some of the tables are now moved to compute the equivalent data on the fly. A second difference is the presence of the new yaw estimation module. Other differences reside in the location of the ADC non-linearity compensation step, that was moved in front of all processing and the on-line computation of various filters. These differences are further discussed below.

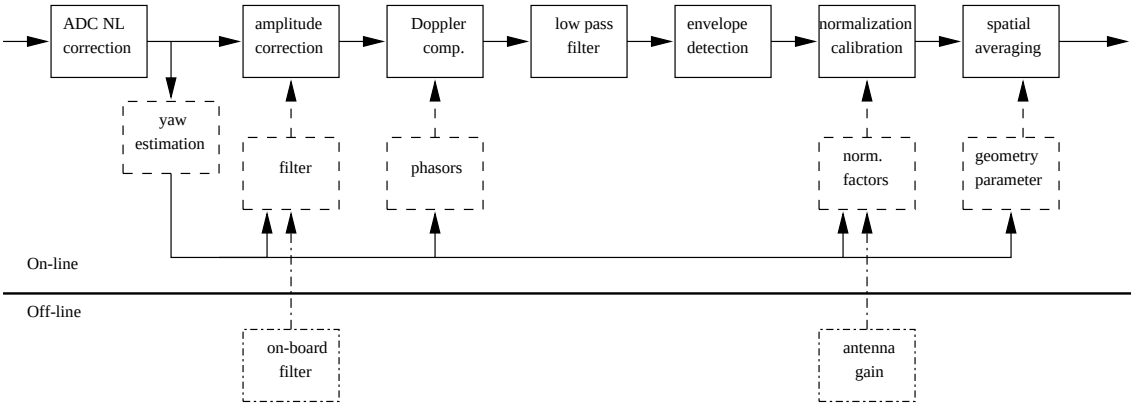

Figure 2. Simplified block diagram of the new processor. This processor does not use any pre-computed tables, mainly because these table could not be pre-computed.

3.2. ADC non-linearity correction

The old processor performed the ADC non-linearity correction of the input data after all the filtering operations. Since the ADC is the last block influencing the signal on-board, the correction of the corresponding non-linearities should be the first operation to be performed when the signal is received on-ground. Considering that the only non-linearity of the chain resides in the on-board ADC characteristic and compensating for the ADC non-linearities, a linear chain between the acquisition and the reception of the data can be assumed.

Moreover, since all the measurements are affected by the ADC non-linear characteristic, the corresponding correction has to be performed on the internal calibration measurement too, while the old processor only corrected the measured echo data and noise power.

3.3. Yaw angle estimation

One of the first tasks of the new processor is to estimate the yaw angle of the spacecraft. Once the yaw angle is known, the acquisition geometry can be computed. This is then used to locate the samples on ground, compute the relative velocity of the corresponding target point and deduce the corresponding per-sample Doppler frequency shift incurred to finally compensate for it.

The yaw angle is estimated from the raw data by measuring the residual Doppler frequency shift. The yaw angle that caused the measured frequency shift is then taken as estimate for the spacecraft's yaw angle. The details of the method are explained below.

3.3.1. Residual Doppler frequency shift measurement

If the on-ground scatterers are assumed uniformly distributed, the spectrum of the returned echo can be assumed to be constant, only modulated by the spectrum of the emitted pulse. The ERS scatterometer being a real-pulse radar, it emits a square pulse modulated around 5.3GHz. The corresponding spectrum is $\sin x/x$-shaped as illustrated in figure 3.

The Doppler frequency shift induced by the relative motion of the on-ground target and the spacecraft is not constant in range, even after the on-board Doppler compensation. Hence, in stead of a simple shift of the spectrum as would be observed if the frequency shift had been constant over range, a deformation of the returned spectrum is observed as is illustrated in figure 3. The corresponding modelling is shown in figure 4.

The mean Doppler frequency shift is measured by computing the best-fit of a Gaussian window onto the spectrum of the received echo. The considered model function is

$$m(f) = ae^{-\frac{(f-f_d)^2}{2\sigma^2}} + n \tag{1}$$

where a is the amplitude, σ is the standard deviation of the Gaussian, n is modelling the additive noise and f_d is the estimated mean Doppler frequency shift. This estimate is more robust than the one based on the computation of the center

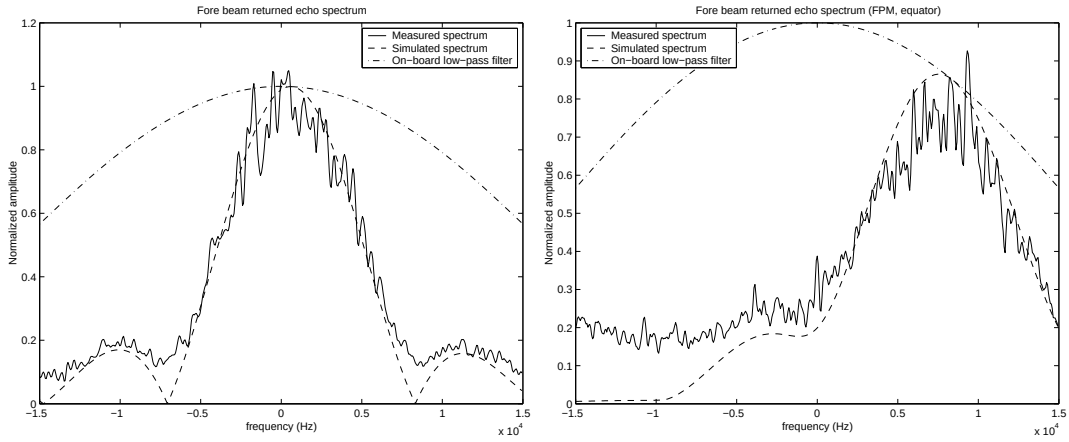

Figure 3. Spectrum of an echo received by the fore-beam antenna. The corresponding pulse length is 130μs. The $\sin x/x$ model is superposed to the real measurement and shows a close match (left). The transmittance of the on-board anti-aliasing filter is also depicted. The graph on the right shows the spectrum of a pulse acquired when the spacecraft was in fine pointing mode (FPM) at the equator. The frequency shift is obvious, as is the deformation of the spectrum due to the range-dependent frequency shift. The superposed model does not take aliasing into account, which explains the differences.

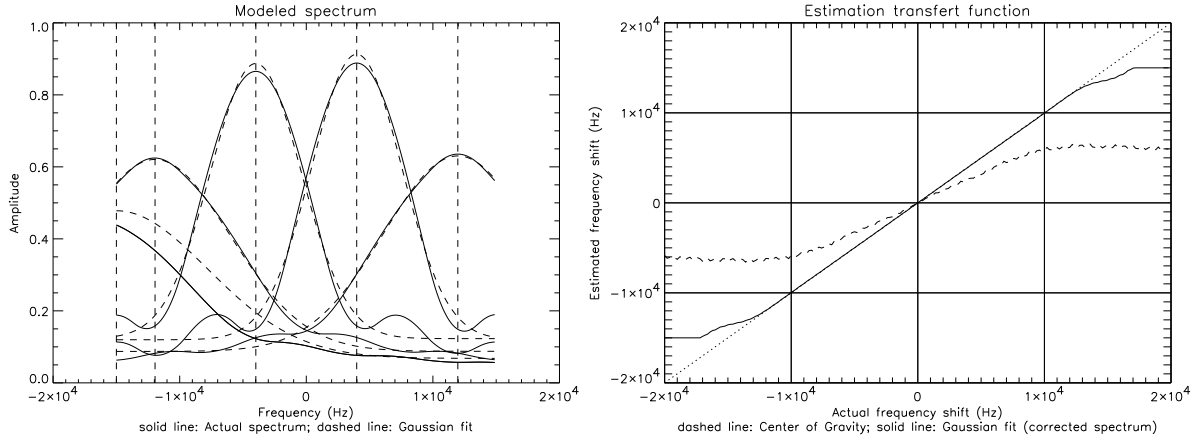

Figure 4. Modelling of the returned spectrum (left). Different across-track evolutions of the Doppler frequency shift are considered. The best matching Gaussian is superimposed on the corresponding spectrum. Validation of the estimation of the Doppler shift (right).

of gravity of the spectrum, particularily when, due to the frequency shift, a major part of the spectrum is shifted outside the anti-aliasing filter bandwidth. The estimation of the mean Doppler frequency shift given for a range-dependent linearily varying Doppler frequency shift is depicted in figure 4. While the Gaussian-fit-based estimator correctly estimates the frequency shift, up to a shift of about 12kHz, the center of gravity estimator is highly biased due to the asymmetry of the spectrum.

3.3.2. Computation of the yaw angle from the frequency shift

To our knowledge, there exists no closed form expression of the Doppler frequency shift for elliptical orbits over an ellipsoidal earth. Therefore, two simplified models were considered. The first model makes the assumption that the relative velocity between the satellite and the Earth target is independent of the yaw angle and yields the following expression for the Doppler frequency

$$f_{\text{Doppler}} = \frac{2\, v_r}{\lambda} \sin\theta \sin(\zeta - \alpha) \tag{2}$$

where v_r is the relative velocity between the satellite and the Earth target, θ is the elevation angle and α is the squint angle of the antenna (0 for a bore-side looking antenna) and ζ is the yaw angle.

The second model considered is drawn from[2] and make the assumption of a circular orbit. The following expression is obtained

$$f_{\text{Doppler}} = \frac{2\,v_{sc}}{\lambda}\sin\theta\cos a\,[1-(\omega_e/\omega)(\cos\beta\sin\Psi\tan a+\cos\Psi)] \tag{3}$$

where v_{sc} is the velocity of the spacecraft along the orbit, λ is the radar wavelength, θ is the elevation angle, a is the angle between the azimuth plane and the plane formed by the spacecraft position and velocity $(\overrightarrow{r_{sc}}, \overrightarrow{v_{sc}})$, ω_e is the Earth's rotation rate, ω is the spacecraft orbital rotation ($\omega = v_{sc}/|\overrightarrow{r_{sc}}|$), β is the argument of latitude (angle measured between the ascending node and the spacecraft position in the orbit plane from the Earth's center) and Ψ is the orbit inclination measured from the Earth spin vector to the orbit rate vector. The yaw angle ζ is related to a by the relation $\zeta = \pi/2+\alpha-a$.

Both equations (2) and (3) are invertible and can yield a closed-form expression of the yaw angle in function of the mean Doppler frequency shift.

Figure 5 presents a comparison of the various approximations to the true Doppler frequency shift w.r.t. the value obtained by simulation along the orbit. The simulation consists in computing the various quantities involved in the expression of the definition of the Doppler frequency shift

$$f_d = \frac{2\,f_t}{c}(\overrightarrow{v_{sc}} - \overrightarrow{v})\cdot\overrightarrow{r_1} \tag{4}$$

where f_t is the carrier frequency, c is the speed of light, $\overrightarrow{v_{sc}}$ is the velocity vector of the satellite, $\overrightarrow{v}$ is the velocity vector of the target on Earth and $\overrightarrow{r_1}$ is the unit vector from the target on Earth to the satellite. The Doppler frequency shift compensation applied on-board is also taken into account in the simulated value. The best approximation seems to be the one deduced from eq. (3).

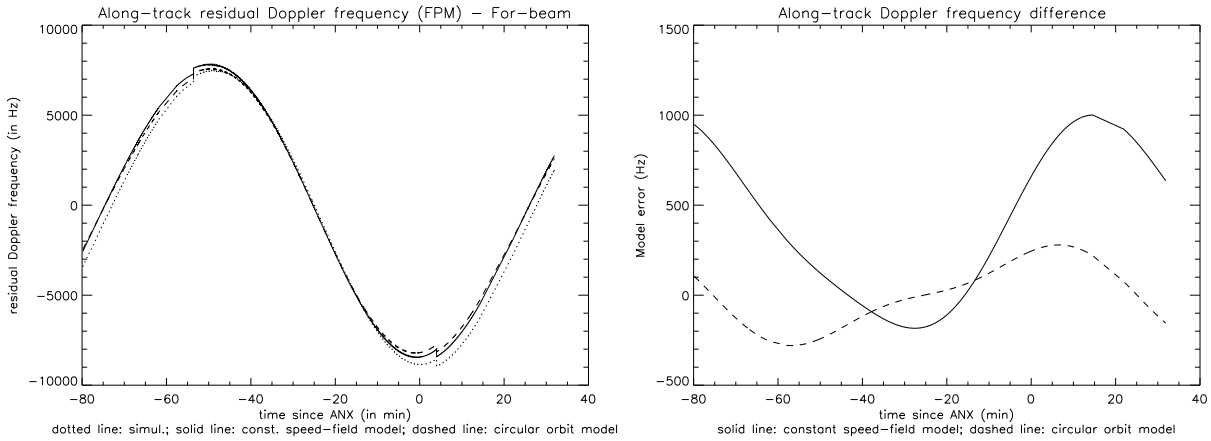

Figure 5. Comparison between the different models and the true value for the residual Doppler frequency shift along an orbit. The satellite pointing was perpendicular to the absolute flight direction (so-called Fine Pointing Mode — FPM) and the yaw error w.r.t. YSM thus varies from -4^o to $+4^o$, is zero at the poles and maximum at the equator. The discontinuity in the graphs are due to a discontinuity in the Doppler compensation function applied on-board. Solid line: the true value from the simulator; dotted line: the residual Doppler frequency shift deduced from eq. (3); dashed line: the residual Doppler frequency shift deduced from eq. (2). The right graph presents the difference of Doppler frequency shift given by corresponding model with the theoretical value.

3.4. Data filtering

There are two main filters involved in the processing of the data. The first filter, called "amplitude correction filter" aims at compensating the characteristic of the on-board anti-aliasing filter while the second filter, called "low-pass filter" aims at reducing the pass-band of the measurement system in order to increase the signal-to-noise ratio.

3.4.1. Amplitude correction filter

If $h(t)$ designates the impulse response of the on-board anti-aliasing filter, $s(t)$ the true backscattered signal and $s_h(t)$ the signal on-board after anti-aliasing filtering but before sampling, one has

$$s_h(t) = h(t) * s(t) \tag{5}$$

where one would like to recover $s(t)$ from (sampled versions of) $s_h(t)$. Due to the presence of noise, (5) should rather be written as

$$s_h(t) = h(t) * s(t) + n(t) \tag{6}$$

where $n(t)$ is the system noise (including the quantization noise) or in the Fourier domain

$$S_h(f) = H(f)S(f) + N(f). \tag{7}$$

This kind of problems where $S(f)$ is to be recovered from a degraded version $S_h(f)$ are termed "Inverse problems"[3] and are known as being ill-conditionned what means that the trivial solution

$$\hat{S}(f) = S_h(f)/H(f) - N(f)/H(f) \tag{8}$$

does not yield usable results if it yields results at all.

The general method to deal with these problems is to regularize them by imposing additional regularity conditions to the solution. By minimizing the expectation of the mean-square error between the actual signal $s(t)$ (unknown) and the estimate $\hat{s}(t)$ one obtains a filter which is called the Wiener filter.[4] The Wiener filter is optimum under the assumptions that 1) the signals (signal and noise) are stationnary (weak stationnarity of the covariance) and 2) the power spectral densities of the original signal and of the noise are known.

Under these assumptions, the Wiener filter is defined as

$$H_w(f) = \frac{H^*(f)P_s(f)}{|H(f)|^2 P_s(f) + P_n(f)} \tag{9}$$

where $P_s(f)$ and $P_n(f)$ are the Power Spectral Densities (PSD) of the original signal and the noise respectively. An estimate of the original signal is thus obtained by

$$\hat{S}(f) = H_w(f)S_h(f) \tag{10}$$

Replacing $S_h(f)$ in (10) by its expression from (7), the global transfer function is obtained

$$\hat{S}(f) = H_w(f)H(f)S(f) + H_w(f)N(f) \tag{11}$$

The product $H_w(f)H(f)$ will be close to 1 where the signal to noise ratio $|H(f)|^2 P_s(f)/P_n(f)$ is large. Where the noise dominates ($P_n(f) \gg |H(f)|^2 P_s(f)$), $H_w(f)$ will be very small and hence filter the noise out.

The expression of the Wiener filter (9) thus depends on the PSD of both the noise and the signal. While the PSD of the noise will be assumed constant, corresponding to a white noise assumption, the PSD of the signal will depend on the spectrum on the received signal. As shown in section 3.3 this spectrum is highly dependent on the residual Doppler frequency shift and hence on the yaw angle. The optimal amplitude correction filter will thus depend on the yaw angle. Figure 6 illustrates these points. While the optimal filter computed for a unshifted pulse exhibits pronounced zeroes at the locations where the signal PSD is itself small, a residual frequency shift not only displaces the dips of the filter, but also reduces their amplitude. It should be noted that the optimum filter is highly different from the one used in the old processor as can be seen in fig. 6.

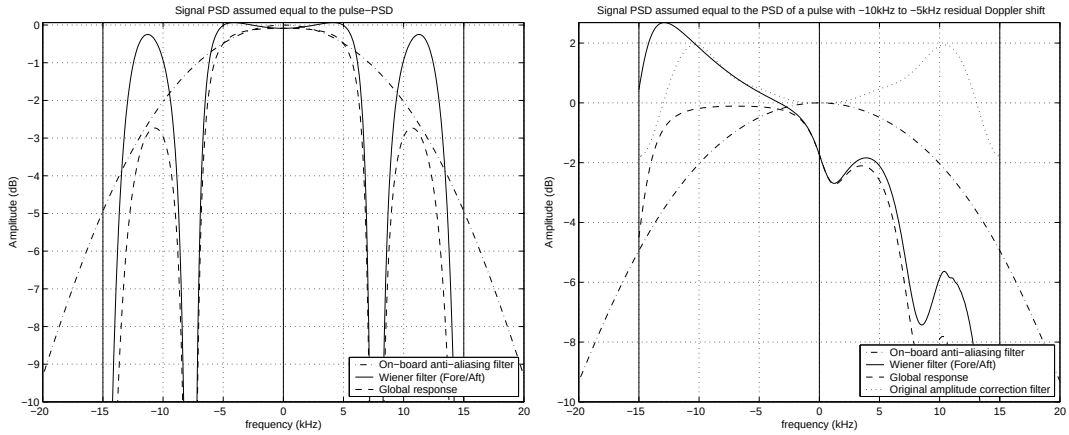

Figure 6. Wiener filter in the case of a signal PSD assumed equal to the emitted pulse PSD (left) and assumed equal to the emitted pulse PSD with a residual Doppler shift ranging from -10kHz to -5kHz across track (right) — Fore/aft beams

3.4.2. Low-pass filter

After compensation of the residual Doppler frequency shift, the signal is filtered again in order to optimize the signal to noise ratio. The goal here is to estimate a signal from a noisy version of it. A similar reasoning as the one held in section 3.4.1 can be followed.

There is no degradation filter here or equivalently, $h(t) = \delta(t)$ and equation (6) becomes

$$s_l(t) = s(t) + n(t). \tag{12}$$

where $s(t)$ is the idealized noise-free signal to be estimated, $n(t)$ represents all the noise sources, including quantization noise and signal model noise. $s_l(t)$ is the actual signal to be filtered. The Fourier transform of the degradation filter is $H(f) = 1$ and the expression for the Wiener filter (9) hence becomes

$$H_w(f) = \frac{P_s(f)}{P_s(f) + P_n(f)} \tag{13}$$

Since the range-dependent residual Doppler frequency shift has been compensed for, the signal to be estimated can be assumed to have a $\sin x/x$-shaped spectrum. The resulting filter is shown in figure 7 together with the original low pass filter. While the SNR is of 10.85dB before filtering, after low-pass filtering with the original filter, it would raise to 11.90dB and using the optimal Wiener filter, one would attain 15.64dB. The reason for this is that the original low-pass filter not only filters the noise out, but also filter some quite powerful signal components, as is illustrated in fig. 7 right and this reflects in the figures mentionned above. The point is that a scatterometer should make precise energy measurements, while classical radar systems rather favour detection probability and raw impulse response shape.

3.5. Enhanced spatial resolution

The current spatial resolution of the nominal ERS scatterometer product is of about 50km in azimuth and in across-track directions. Accordingly, the backscattering coefficients are provided on a 25km-spacing regular grid of nodes. The σ^0 values at the nodes are obtained by spatially averaging the measurements using a separable Hamming weighting function. This averaging is performed in order to have a uniform spatial resolution and to reduce the variance of the σ^0 values.

The spatial resolution of the raw measurements is not infinite and is limited by two factors. The azimuth spatial resolution is governed by the projection of the azimuth antenna pattern on ground. Similarly, the across-track resolution on ground depends on the projection of the emitted pulse on ground and on the pass-band of the system. Both factors hence depend respectively on the elevation angle of the target in the antenna beam and on the incidence angle of the signal on ground.

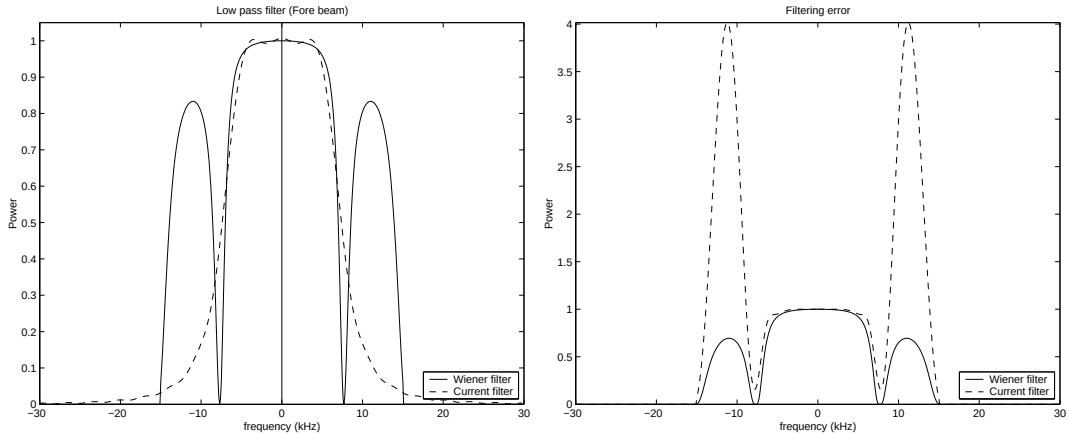

Figure 7. Original low-pass filter and new optimal Wiener filter for a Fore-beam pulse (left). Filtering error due to each type of filter (right).

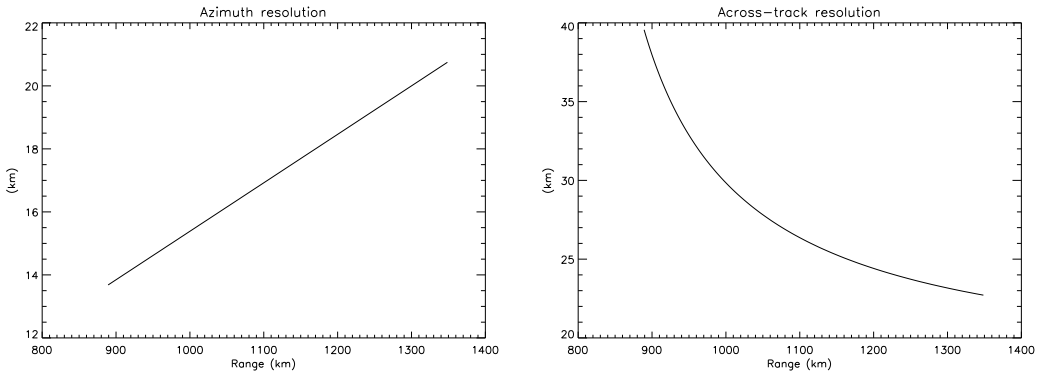

Figure 8. Spatial resolution of the raw measurements respectively in azimuth (left) and across-track in function of the range of the target (right)

The high-resolution product is obtained by reducing the size of the averaging window and decreasing the node spacing to approximately 12.5km. An optimization of the resolution over land using super-resolution methods and data comming from several passes[5–7] was not considered.

An analysis of the aliasing due to the higher spatial resolution is now in order. The inherent along-track sampling of the measurements leads to aliasing, the antenna gain pattern being used as a kind of anti-aliasing filter. The worst case in that concern is the mid-beam near range case at the south pole (perigee), were the antenna footprint has the smallest along-track extend on ground. The one-way along-track cut in the antenna gain pattern is closely approximated by the expression

$$G_a(\phi) = \frac{\sin^2 \alpha\phi}{(\alpha\phi)^2} \tag{14}$$

where $\alpha = 130$ is a constant. The corresponding spectrum is triangular-shaped and vanishes for spatial frequencies $k_\phi > \alpha/\pi$. Making the assumption of the small angles $\phi \ll 1$, the impulse response function of a point target located at range R and azimuth y is given by

$$G_a^2(y/R) = \frac{\sin^4 \alpha y/R}{(\alpha y/R)^4}. \tag{15}$$

Measurements are made every 941ms or approximately every 6.25km. This leads to an aliasing of the measurements as shown in the left part of figure 9. This aliasing error leads to a signal to noise ratio of about 51dB and can thus be neglected. For larger ranges, the aliasing error is even totally null since the spectrum of the azimuth antenna gain pattern

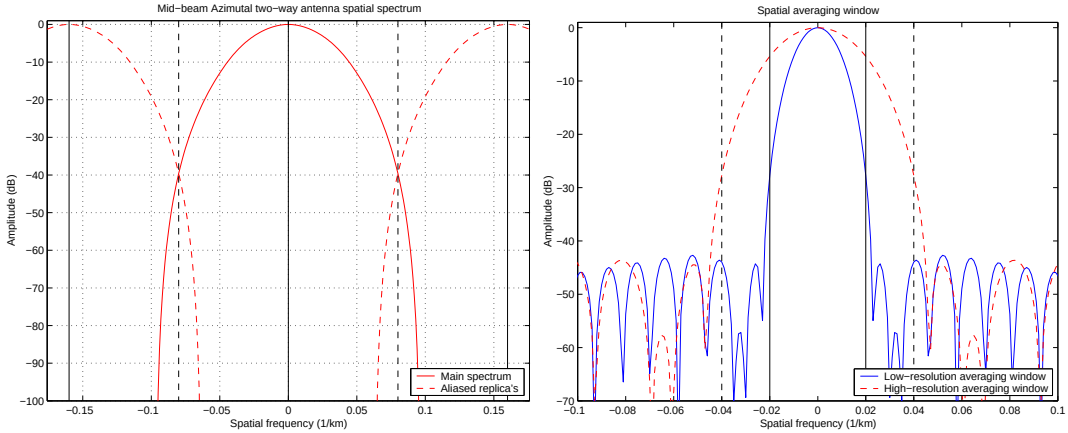

Figure 9. Left: Aliasing due to the along-track sampling. The range considered was 855km and corresponds to the near-swath case at the south pole. The vertical dashed lines represent the Nyquist frequency of 1/12.5km. Right; Spatial spectrum of the nominal and high resolution averaging Hamming window. The vertical lines represent the Nyquist frequency for the corresponding spatial sampling (sampling frequency of resp 1/25km or 1/12.5km).

has a finite extend. Moreover, the error signal corresponding to the aliasing error is filtered out by the subsequent low-pass filter (see below).

The right part of figure 9 shows the spectrum of the spatial averaging windows at nominal and at high resolution. The corresponding spatial sampling will also lead to aliased energy. In this case, the SNR is found to be respectively of 42dB and 47dB and the aliased energy is thus also negligible. The SNR in the high resolution case is higher than the SNR in the nominal resolution for several factors. The main lobe of the spatial filter is twice larger and moreover is not large enough to include energy aliased from the tails of the along-track antenna gain pattern spectrum.

This shows that the spatial resolution enhancement does not decrease the SNR due to aliasing problems. However, the number of averaged individual measurements will be roughly 4 times smaller, which will have an impact on the variance of the corresponding σ^0.

4. CONCLUSIONS

After gyroscopes malfunctions, a new gyro-less piloting mode was introduced on the ERS-2 spacecraft. The existing ground processor for the ERS-2 scatterometer data is not able to handle data acquired in the new attitude. This prompted for a review of the processing chain.

The new processing chain, that unlike the old processor, does not rely at all on pre-computed look-up tables was described. Some of the functional modules were kept untouched, others such as the ADC non linearity correction were moved earlier on the signal path. A new module was introduced to perform the estimation of the — now unknown — yaw angle and other time- and spatial filtering modules were modified.

The method used to estimate the attitude was described. It is based on the measurement of the residual Doppler frequency shift. The expression of the new optimal Wiener-filter in the time-filtering modules was derived. The performance of these new filters were compared to the existing ones. Finally, an evaluation of the eventual impact of the increased resolution on the signal to noise ratio was conducted and shown to be negligible from a signal processing point of view. However, the signal variance will increase since the number of averaged measurements is smaller.

The results of the validation of these modifications are reported in another article[8] in these proceedings.

ACKNOWLEDGMENTS

This work was performed under European Space Agency (ESA) contracts. We would like to thank the ESA for the use of data and the provision of industry-confidential information. This work would not have been possible without the help of Pascal Lecomte and Raffaele Crapolicchio from the European Space Agency/ESRIN.

REFERENCES

1. P. Lecomte, "The ers scatterometer instrument and the on-ground processing of its data," in *Proceedings of a Joint ESA-Eumetsat Workshop on Emerging Scatterometer Applications – From Research to Operations*, pp. 241–260, ESTEC, (The Netherlands), Nov. 1998.
2. R. K. Raney, "Doppler properties of radars in circular orbits," *Int. J. Remote Sensing* **7**, pp. 1153–1162, Sept. 1986.
3. A. K. Katsaggelos, *Digital Image Restoration*, Springer-Verlag, 1991.
4. H. C. Andrews and B. R. Hunt, *Digital Image Restoration*, Prentice Hall, Inc., Englewood Cliffs, New-Jersey, USA, 1977.
5. D. Early, D. Long, and T. Stein, "Scatterometer resolution enhancement," in *Geoscience and Remote Sensing Symposium Proceedings, IGARSS '98*, pp. 1970–1972, 1998.
6. J. A. Perez, S. Marshall, C. Schmullius, M. Habermeyer, and K. Gregson, "Resolution enhancement of ers scatterometer data," in *Proceedings of a Joint ESA-Eumetsat Workshop on Emerging Scatterometer Applications – From Research to Operations*, pp. 57–62, ESTEC, (The Netherlands), Nov. 1998.
7. D. G. Long, P. J. Harding, and P. T. Whiting, "Resolution enhancement of spaceborne scatterometer data," *IEEE Trans. on Geoscience and Remote Sensing* **31**, pp. 700–715, May 1993.
8. P. Pettiaux, X. Neyt, and M. Acheroy, "Validation of the ers-2 scatterometer ground processor upgrade," in *Proceedings of SPIE: Remote Sensing of the Ocean and Sea Ice 2002*, **4880**, 2002.